Monthly Notices of the ROYAL ASTRONOMICAL SOCIETY

MNRAS **526,** 106–117 (2023) https://doi.org/10.1093/mnras/stad2670
Advance Access publication 2023 September 06

A LOFAR prompt search for radio emission accompanying X-ray flares in GRB 210112A

A. Hennessy [1★] R. L. C. Starling [1] A. Rowlinson [2,3] I. de Ruiter [2] A. Kumar,[4] R. A. J. Eyles-Ferris,[1] A. K. Ror,[5] G. E. Anderson [6] K. Gourdji [7,8] A. J. van der Horst,[9] S. B. Pandey,[5] T. W. Shimwell,[3,10] D. Steeghs [4] N. Stylianou,[1†] S. ter Veen,[3] K. Wiersema[11,12] and R. A. M. J. Wijers [2]

[1]*School of Physics and Astronomy, University of Leicester, University Road, Leicester LE1 7RH, UK*
[2]*Anton Pannekoek Institute for Astronomy, University of Amsterdam, Science Park 904, NL-1098 XH Amsterdam, the Netherlands*
[3]*ASTRON, the Netherlands Institute for Radio Astronomy, Oude Hoogeveensedijk 4, NL-7991 PD Dwingeloo, the Netherlands*
[4]*Department of Physics, University of Warwick, Coventry CV4 7AL, UK*
[5]*Aryabhatta Research Institute of Observational Sciences (ARIES), Manora Peak, Nainital 263002, India*
[6]*International Centre for Radio Astronomy Research, Curtin University, GPO Box U1987, Perth WA 6845, Australia*
[7]*Centre for Astrophysics and Supercomputing, Swinburne University of Technology, Hawthorn VIC 3122, Australia*
[8]*OzGrav: ARC Centre of Excellence for Gravitational Wave Discovery, Hawthorn VIC 3122, Australia*
[9]*Department of Physics, George Washington University, 725 21st St NW, Washington, DC 20052, USA*
[10]*Leiden Observatory, Leiden University, PO Box 9513, NL-2300 RA Leiden, the Netherlands*
[11]*Centre for Astrophysics Research, University of Hertfordshire, Hatfield AL10 9AB, UK*
[12]*Physics Department, Lancaster University, Lancaster LA1 4YB, UK*

Accepted 2023 August 31. Received 2023 August 30; in original form 2023 July 7

ABSTRACT

The composition of relativistic gamma-ray burst (GRB) jets and their emission mechanisms are still debated, and they could be matter or magnetically dominated. One way to distinguish these mechanisms arises because a Poynting flux dominated jet may produce low-frequency radio emission during the energetic prompt phase, through magnetic reconnection at the shock front. We present a search for radio emission coincident with three GRB X-ray flares with the LOw Frequency ARray (LOFAR), in a rapid response mode follow-up of long GRB 210112A (at $z \sim 2$) with a 2 h duration, where our observations began 511 s after the initial *Swift*-BAT trigger. Using time-sliced imaging at 120–168 MHz, we obtain upper limits at 3σ confidence of 42 mJy averaging over 320 s snapshot images, and 87 mJy averaging over 60 s snapshot images. LOFAR's fast response time means that all three potential radio counterparts to X-ray flares are observable after accounting for dispersion at the estimated source redshift. Furthermore, the radio pulse in the magnetic wind model was expected to be detectable at our observing frequency and flux density limits which allows us to disfavour a region of parameter space for this GRB. However, we note that stricter constraints on redshift and the fraction of energy in the magnetic field are required to further test jet characteristics across the GRB population.

Key words: gamma-ray burst: individual: GRB 210112A – X-rays: bursts – radio continuum: transients.

1 INTRODUCTION

Gamma-ray bursts (GRBs) show a broad range of spectral and temporal behaviours, but are generally classified into two main categories. GRBs are defined by their spectral hardness and T_{90} (the time for 5 per cent to 95 per cent of photons to be detected). Long gamma-ray bursts (LGRBs) are spectrally softer than their short gamma-ray burst (SGRB) counterparts, and have $T_{90} \gtrsim 2$ s. LGRBs are the most common class (Kouveliotou et al. 1993) and occur during the deaths of massive stars in core-collapse supernova, many have been associated with Type Ic supernova (Galama et al. 1998; Hjorth et al. 2003). SGRBs, on the other hand, are shorter in duration and are expected to occur during a binary neutron star (NS-NS) or neutron star-black hole mergers (Lattimer & Schramm 1976; Abbott et al. 2017). This work presents observations of an LGRB.

Relativistic jets are formed in the collapse (Woosley & MacFadyen 1999), and if pointed towards Earth, we observe an intense series of one or more gamma-ray pulses lasting a few ms to a few hundred seconds. The pulses are attributed to internal shocks or magnetic reconnection events, close to the progenitor of the burst (Rees & Meszaros 1994). The GRB jet cannot be directly resolved, and the composition and emission mechanisms still remain an open question in GRB physics. There are models supporting both a matter-dominated (Rees & Meszaros 1994) or a magnetically dominated (Drenkhahn & Spruit 2002) jet.

★ E-mail: ah724@leicester.ac.uk
† Present address: Department of Physics, University of Oxford, Denys Wilkinson Building, Keble Road, Oxford OX1 3RH, UK.

As the jet propagates from the progenitor it will collide with intermediate matter and produce a unique afterglow. The properties of these are described by synchrotron, inverse Compton or synchrotron self-Compton emission, which results in broken power-law behaviour both temporally and spectrally, these have been observed from X-ray to GHz radio (Costa et al. 1997; Frail et al. 1997; van Paradijs et al. 1997). GeV emission is also attributed to the afterglow (Abdo et al. 2009). The *Neil Gehrels Swift Observatory* (hereafter *Swift*, Gehrels et al. 2004) detects X-ray afterglows in 95 per cent of GRBs it detects (Evans et al. 2009).

Flares are often observed superimposed on the X-ray afterglow, usually in the first few hundred seconds. These flares show a variety of temporal features similar to the prompt emission (Guidorzi et al. 2015). X-ray flares and gamma-ray pulses can be seen coincident in a number of bursts; and many studies favour that both have the same internal origins (e.g. Chincarini et al. 2007; Falcone et al. 2007; Hu et al. 2014). There are a number of theories on the exact origins of these flares, including the late internal-shock model (Fan & Wei 2005), late time energy injection (Nousek et al. 2006) and misaligned jets (Duque et al. 2022). Pulses and flares have been shown to share the same power-law distribution of peak flux, duration, and waiting time as Solar flares, suggesting that both may form through a similar magnetic process in very different environments.

The magnetic reconnection process is capable of releasing quick, powerful bursts of energy, making it a suitable candidate to power GRB prompt emission. It has also been shown capable of producing the inherent variability in light curves (Beniamini & Granot 2016). In this paper, we aim to test a magnetically dominated jet model. At least one magnetic model produces a testable prediction of short pulses of coherent radio emission corresponding to gamma-ray pulses, but observed with a delay due to dispersion (Taylor & Cordes 1993). Electromagnetic radiation is spread and slowed as it propagated through the intergalactic medium (IGM); and interstellar medium in the host galaxy and the Milky Way. Longer wavelengths are affected more, thus we see radio signals at a delay compared to X-ray. Radio emission should occur at the shock front of a relativistic, magnetized wind as it interacts with ambient media, with a peak frequency at most a few MHz, well below the capabilities of current facilities. However, radio facilities such as the LOw Frequency ARray (LOFAR, van Haarlem et al. 2013) can still detect the high frequency tail of this emission. LOFAR's rapid response is not fast enough to observe most prompt gamma-ray flares, rather Starling et al. (2020) proposed a probe of the more accessible late-time X-ray flares. These occur on time-scales typically reachable with the LOFAR rapid response mode capability of $\sim$5 min. They also show that of a sample of 200 flares from 81 *Swift* GRBs, 44 per cent of flares would have been observable at 144 MHz using LOFAR's rapid response mode ($\leq$5 min) if generated in a magnetically dominated wind as described by Usov & Katz (2000). These flares occur in both long and short GRBs so we may expect to see these signals in all GRBs that have the correct flare characteristics. Demonstrating that radio signals produced analogous to prompt gamma-ray pulses and X-ray flares, and hence directly linked to central engine activity, would provide great evidence for a Poynting flux dominated emission mechanism in GRBs.

The radio signals in aforementioned model are powered by the same central engine activity that produces currently observable gamma-ray pulses or X-ray flares. Demonstrating that radio signals produced analogous to these features, and hence directly linked to central engine activity, would provide great evidence for a Poynting flux dominated emission mechanism in GRBs.

Coherent radio signals are also predicted as persistent emission and short pulses during the formation of a magnetar (Zhang & Mészáros 2001; Rowlinson & Anderson 2019). Some models predict SGRBs to form a magnetar in the burst event – emission is expected during spin-down and subsequent collapse into a black hole (Zhang 2014). This may also apply for LGRBs, if a magnetar can be formed (Bernardini 2015). The short pulses are likely to look like, and may contribute to, the population of Fast Radio Bursts (FRBs), another class of transient event characterized by short pulses of radio emission. These models postulate that at least some FRBs may occur from SGRBs (Totani 2013; Gourdji et al. 2020). A possible (2.8σ) associated of an NS-NS merger and FRB was recently reported through a comparison between public gravitational wave and CHIME FRB data, where the FRB could be attributed to the magnetar collapse (Moroianu et al. 2023). An association would explain the origin of at least some FRBs, and would be a powerful probe of neutron star mergers.

There have been a number of previous searches for prompt radio emission from GRBs, but often due to a lack of sensitivity or response time, it has proven difficult to obtain a detection (Koranyi et al. 1995; Dessenne et al. 1996; Anderson et al. 2018).

Recent follow-up observations using LOFAR looked to test models of the formation of a magnetar. Rowlinson et al. (2019) followed-up an LGRB beginning 4.5 min after the event, finding a 3σ upper limit of 1.7 mJy beam^{-1} for the full 2 h 120–168 MHz observation, and finding no detection of burst-like emission in time-sliced data with cadence ranging from 10 min down to 30 s. This is the deepest low frequency limit to date, to our knowledge. A similar 120–168 MHz follow-up of an SGRB finds a 3σ limit of 153 mJy on emission during the plateau phase with 136 s integrated images (Rowlinson et al. 2021). This limit is two orders of magnitude greater than the predicted radio flux at the putative host redshift of 1.8, and they constrain the efficiency of rotational energy conversion into coherent radio emission to be $\leq 6 \times 10^{-8}$.

The Murchison Widefield Array (MWA, Tingay et al. 2013; Wayth et al. 2018), a low-frequency radio facility in the Southern hemisphere, whilst not able to reach the same flux limits as LOFAR, has the advantage of a very rapid response of $\sim$20 s to a burst trigger, allowing it to probe the earliest times after a burst. A follow-up of an LGRB found no detection of pulse-like emission, acquiring fluence upper limits of 77–224 Jy ms corresponding to 0.5–10 ms pulse widths, some of the most stringent to date (Tian et al. 2022b). A search for emission analogous to X-ray flares was also conducted and the non-detection helped establish constrains on the fraction of magnetic energy. Investigations of short GRBs with MWA also have so-far found no detection of radio emission (Kaplan et al. 2015; Anderson et al. 2021; Tian et al. 2022a).

Here, we present a search for prompt coherent radio emission coincident with high energy flaring in long GRB 210112A. This burst was observed as part of a LOFAR High Band Antenna (HBA) rapid-response campaign, and is a promising candidate for testing magnetic wind modes due to several prominent and simultaneous gamma-ray pulses and X-ray flares, continuing to a time accessible by LOFAR (i.e. >5 min after burst). Section 2 details the observations with *Swift*, LOFAR, and ground-based optical telescopes used in this study. In Section 3, we model the X-ray flares and place GRB 210112A in the context of the *Swift* GRB afterglow sample. Section 4 outlines the magnetic wind model which these observations can test, and we make predictions for the observable flux density at 144 MHz with LOFAR. We present the results of our radio search in Section 4.2, and in Section 5 we examine the assumed redshift, discuss the implications of our findings on jet and progenitor models and look to future LOFAR upgrades, concluding in Section 6. Errors are stated as 1σ confidence unless otherwise stated.

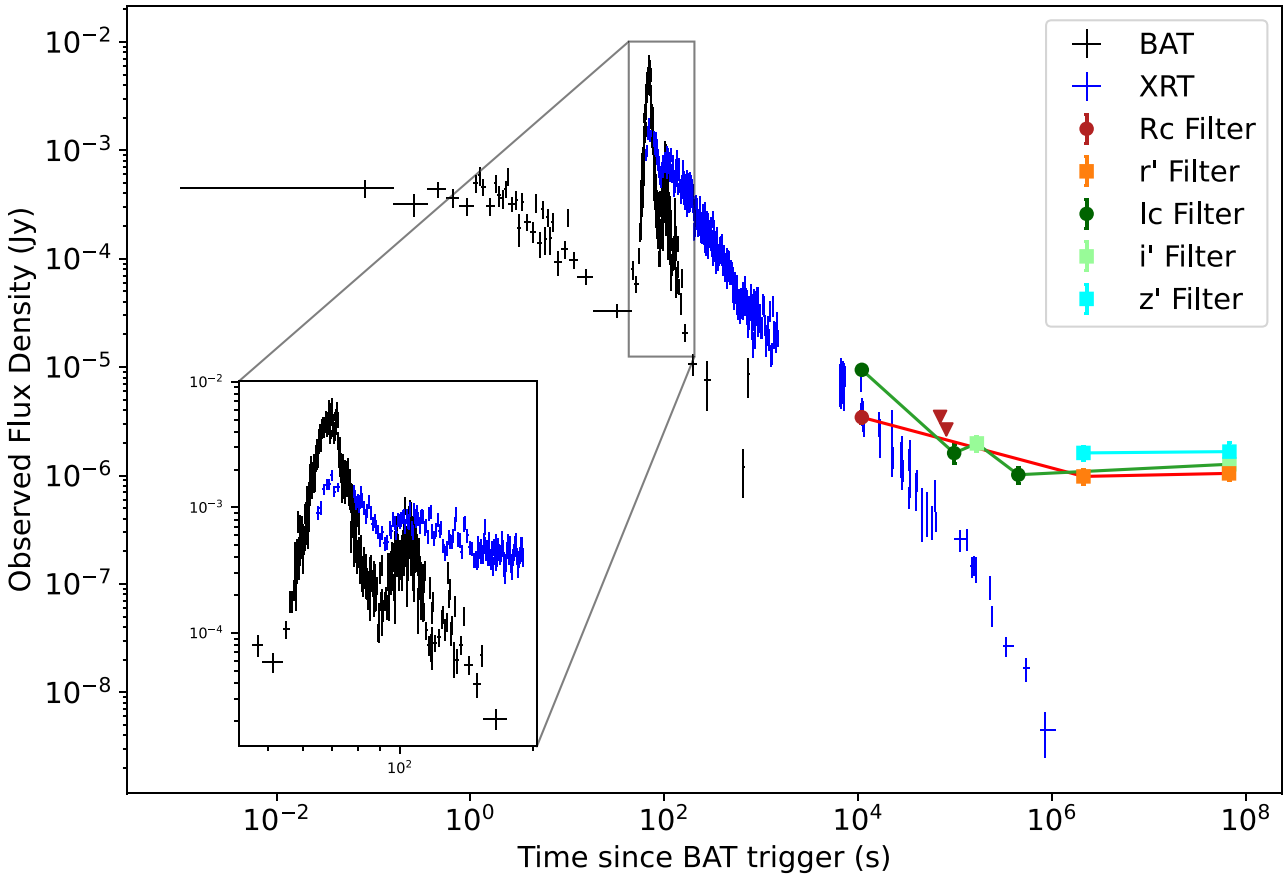

Figure 1. The observed flux density light curve of all *Swift*-BAT (at 50 keV) and *Swift*-XRT (at 1 keV) data, and ground-based optical data used in this paper, showing coincident gamma-ray pulses and X-ray flares. The black data points are BAT, and blue represents the XRT data. Optical data (green, orange, purple) come from OSN, Mondy, DFOT, CAHA, DOT, and LBT. See Section 2 for references and Table C1 for full optical data. Inset: a zoom on the main pulsing activity between T + 40 and T + 190 s.

2 OBSERVATIONS AND DATA REDUCTION

GRB 210112A occurred on 2021 January 12 at 01:51:00 GMT, triggering *Swift* (Ambrosi et al. 2021) and several other gamma-ray observatories: AGILE (Astro-Rivelatore Gamma a Immagini Leggero, Ursi et al. 2021); Konus-Wind (Svinkin et al. 2021); Insight-HXMT (Insight-Hard X-ray Modulation Telescope, Zheng et al. 2021). The burst fits into the LGRB category with a T_{90} of 107.6 ± 13.0 s in the 15–350 keV energy range (Stamatikos et al. 2021).

Follow-up was conducted at X-ray (Evans et al. 2021; Goad et al. 2021), ultraviolet, and optical wavelengths [Siegel, Ambrosi & Swift/UV-Optical Telescope (UVOT) Team 2021] by *Swift* and a number of ground-based optical facilities: Kitab (Novichonok et al. 2021), OSN (Sierra Nevada Observatory, Kann et al. 2021a, b), DFOT (Devasthal Fast Optical Telescope, Gupta et al. 2021), Mondy (Pankov et al. 2021), CAHA (Calar Alto Observatory, Kann et al. 2021c), DOT (Devasthal Optical Telescope, Dimple et al. 2021; Misra et al. 2021), LBT (Large Binocular Telescope, Rossi, CIBO Collaboration & Kann 2021). Our rapid-response LOFAR observations were automatically triggered, and LOFAR HBA began observing the target shortly after the X-ray position was reported, the GRB position being immediately available for LOFAR, 511 s after the burst.

Subsequent sections detail the observations and methods of analysing the data. The gamma-ray, X-ray, and optical data used in this work are shown together in Fig. 1. BAT and XRT (X-ray Telescope) are plotted at 50 and 1 keV, respectively (Evans et al. 2010). Optical data are plotted at the central frequency of each filter, accounting for a Galactic extinction according to Schlafly & Finkbeiner (2011).

2.1 *Swift*

The Burst Alert Telescope (BAT, Barthelmy et al. 2005) on board *Swift* was triggered at 01:37:03 UT, 2001 January 12. On detection, the observatory slewed and the XRT (Burrows et al. 2005) began observing 74.2 s after the initial BAT trigger, finding an uncatalogued X-ray source at RA, DEC (J2000) = 14^{h} 36^{m} 1.06^{s}, + 33°03′23.8″ (90 per cent error radius 1.4″). 83 s after the initial trigger, the UVOT (Roming et al. 2005) began observing and detected a source in the White filter with a 147 s exposure. The detection was accumulated in an image spanning more than the duration of the prompt emission, so is not utilized further. The *V, B, U*, and *UVW1* filters were also used at later times, but no source was detected in these images and only upper limits were derived (Siegel et al. 2021).

We obtained the data from the online *Swift* archive[1] at the UK Swift Science Data Centre (UKSSDC, see Evans et al. 2009). Data

[1] https://www.swift.ac.uk/swift_portal/

reduction and spectral analysis were carried out in HEASOFT[2] [version 6.31.1, Nasa High Energy Astrophysics Science Archive Research Center (Heasarc) 2014] and XSPEC (version 12.13, Arnaud 1996).

2.1.1 Swift-*BAT*

The light curve presented in Fig. 1 demonstrates several gamma-ray pulses over the observation. The spectral data were extracted with the BATBINEVT pipeline. The data were timesliced according to visually identified pulses and availability of overlapping XRT data, described in Table A1. The BAT spectral data were modelled with a cutoff power law, where the photon index, exponential cutoff, and normalization were free parameters.

2.1.2 Swift-*XRT*

The light curve uses data from all three modes of *Swift* operation: slewing, windowed timing, and photon counting.

The spectral data in windowed timing and photon counting modes were timesliced as defined by Table A1, beginning at the decay of the first flare. Each timeslice was fitted with one of several models.

For periods where there is no overlap between BAT and XRT data, a power law with two components of absorption was fitted (Wilms, Allen & McCray 2000). The first component models the line-of-sight absorption through our own Galaxy with the column density calculated from Willingale et al. (2013) based on the location of the GRB, and this remains fixed across the full time interval of the GRB. For the position of GRB 210112A, this gives a value of $N_{\rm H,Gal} = 9.55 \times 10^{19}\,{\rm cm}^{-2}$. The second absorption parameter is an intrinsic component due to absorption in the line-of-sight IGM and host galaxy of the GRB source. This should also remain constant through the observation, as the parameter is not directly linked to the burst itself. Thus, we first create a late time spectrum ($T + 8913$ to $T + 1.7 \times 10^5$) with this parameter allowed to vary. We select late time data as the burst is less energetic at this point – the time-scale and magnitude of variability is smaller in the afterglow. We find a value of $N_{\rm H,host} = 2.98\,(\pm 0.33) \times 10^{22}\,{\rm cm}^{-2}$ (90 per cent confidence interval) and freeze this for all other spectral fits. A tentative redshift value of $z \sim 2$ is reported in Kann et al. (2021a) which we include as a frozen value, though we acknowledge it is an estimate. We revisit this value in Section 5. For periods of overlapping BAT and XRT data, we fit the absorbed broken power-law model, with absorption described as above, and a spectral energy break allowed to vary, which in all three joint fits remained at ∼13.5 keV.

The spectral evolution of power-law indices is shown in Fig. 2. The low-energy and the high-energy indices represent the spectral indices before and after the energy break, respectively, and where there is not a joint model, simply represent the spectral index of the fitted XRT or BAT data. Both spectral indices evolve as expected in a GRB – the spectrum is initially hard during the energetic initial stages of the burst, but rises to $\Gamma \sim 2$ during the afterglow.

2.2 LOFAR

At 01:45:35 UTC, LOFAR triggered on GRB 210112A in Rapid Response Mode obtaining 7199 s of observation on target, starting 511 s after the initial *Swift*-BAT trigger (project code LC15_013). Observations were made with LOFAR HBA that operate in the

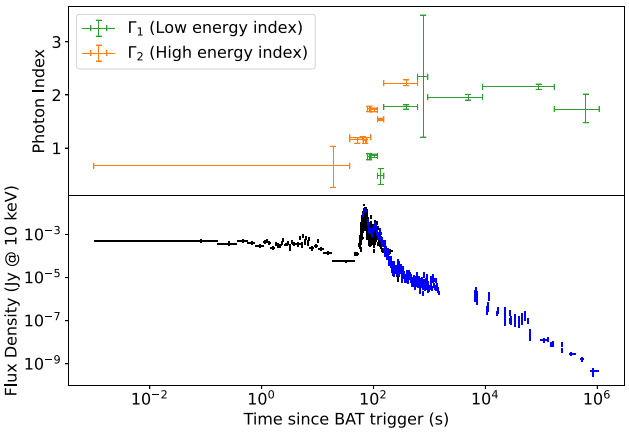

Figure 2. The spectral evolution of the power-law index parameters, for each timeslice of data. Where there is combined data, Γ_1 is the low-energy photon index and Γ_2 the high-energy counterpart. Otherwise, they are the BAT fitted power law and XRT fitted power law, respectively. The full set of timeslices and fit parameters are tabulated in Table A1. Error in photon index is the fitted parameter 90 per cent confidence interval. Bottom: combined BAT and XRT flux density (extrapolated to 10 keV) light curve, for reference.

120–168 MHz frequency range. The data were averaged with a 1 s integration time and 244 sub-bands with a bandwidth of 195.3 kHz (16 channels per sub-band). 23 core stations and 11 remote stations were used (the Dutch array). After the target observations were completed, a 10 min calibrator observation was taken using 3C147 with the same time and frequency averaging.

We calibrated the data using the LINC[3] pipeline (version 4.0), a pipeline to correct for instrumental effects in LOFAR observations, with 8 s time averaging. Standard LOFAR software and methods are used as described in van Weeren et al. (2016), de Gasperin et al. (2019), and Williams et al. (2016). The pipeline uses the calibrator data to derive direction independent gain solutions. These solutions are applied to the target data and an initial step of phase-only calibration is applied using a sky model from TGSS ADR (Intema et al. 2017). Part of the pipeline includes AOFLAGGER (version 3.2.1, Offringa et al. 2010; Offringa, van de Gronde & Roerdink 2012), enabling statistical flagging and removal of data affected by radio interference. Further direction dependent calibration was not required in our case, as the target GRB position lies at the centre of the observation field.

The calibrated data were imaged using the WSCLEAN (version 3.1.1, Offringa et al. 2014). A large-scale, deep image was created using the full time, full frequency range observation. A 5 arcsec pixel scale was used, and standard imaging parameters included a Briggs weighting −0.5 and auto-thresholding up to 100 000 iterations. Timesliced images were created for 60 and 320 s length time bins, with the same imaging parameters as before, using the full frequency range and a 1 arcsec pixel scale. Subtraction imaging was attempted by subtracting the calculated model visibilities from the target data, but we saw negligible improvement on the rms noise of the images.

2.3 Optical observations

An optical counterpart was detected in several ground-based facilities – see Table C1. Using optical follow-up data collected 3 h after the GRB with the Sierra Nevada Observatory, Kann et al. (2021a) fit a

[2]http://heasarc.gsfc.nasa.gov/ftools

[3]https://git.astron.nl/RD/LINC

spectral energy distribution (SED) consistent with a large amount of Milky Way like dust at $z \sim 2$.

A flattening in the optical light curves was noted in General Coordinates Network (GCN) Circulars and attributed to the host galaxy (Kann et al. 2021c;Rossi et al. 2021). To confirm the host galaxy magnitudes, we obtained further photometry of the GRB 210112A field. The observations were carried out using the ARIES-Devasthal Faint Object Spectrograph and Camera (ADFOSC, Omar et al. 2019) mounted at the 3.6m Devasthal Optical Telescope (Kumar et al. 2018).

Imaging observations in the SDSS *r'* and *i'* bands (300 s × 10 frames and 300 s × 10 frames, respectively) were taken on 2023 February 21, and observations in the *z'* band (300 s × 15 frames) were taken on 2023 March 27; more than two years since the burst.

Pre-processing of the raw data (bias, flat, and cosmic-ray correction) was carried out according to standard procedure. The multiple frames observed on the same night were aligned and stacked to achieve a good signal-to-noise ratio. The host galaxy of GRB 210112A is detected clearly within the 3-σ limit in the stacked frames of *r'*, *i'*, and *z'* bands.

The photometric analysis is conducted using Source Extraction and Photometry (Barbary 2018), a PYTHON Package built on the Source-Extractor (SEXTRACTOR, Bertin & Arnouts 1996) software suitable for performing faint-galaxy photometry, and Sloan Digital Sky Survey (SDSS) standard stars were used to perform the calibration. The estimated calibrated *r'*, *i'*, and *z'* band magnitudes of the host galaxy of the GRB 210112A are 23.89 ± 0.12, 23.67 ± 0.24 and 23.35 ± 0.25 AB mags, respectively, before accounting for the expected Galactic extinction of $E(B - V) = \sim 0.01$ (Schlafly & Finkbeiner 2011).

3 X-RAY FLARE ANALYSIS

In order to generate predictions for prompt radio emission, discussed later in Section 4, we need to calculate the fluences of the X-ray flares. We have developed a code that can model GRB temporal behaviour as a power-law afterglow plus flares. An outline of this process is described in the subsequent section, but will be detailed fully in a future paper.

3.1 Light-curve fitting procedure

The program uses light-curve data made available on the *Swift* Online Archive. The initial step is to identify potential flares, before refining these into a set of start, stop, and peak times. Possible flares are identified by looking for trends where the flux increases in at least 2 out of 3 consecutive data points from point n - additionally each increase must be by a factor of greater than twice the point n's 90 per cent confidence interval. This criterion is somewhat arbitrary, but shows consistent success upon visual inspection. For each potential flare, we find the start and peak by finding the local minima and maxima, respectively. Identifying the end of the flare is a more involved process as it fades into the afterglow. We based our method on Evans et al. (2009). For each point we calculate two decay indices, $\alpha_{\rm peak}$, the gradient from the flare peak to point n; and $\alpha_{\rm next}$, the gradient from point n to $n + 1$. For the decay to end, we require two conditions to be met at least six times over any 10 consecutive points. Condition 1 requires that $\alpha_{\rm peak} > \alpha_{\rm next}$, the gradient from n to $n + 1$ is shallower than gradient from peak to n. Condition 2 requires that $\alpha_{\rm peak}$ and $\alpha_{\rm next}$ are greater in bin n compared to bin $n - 1$, both indices are shallowing over consecutive points.

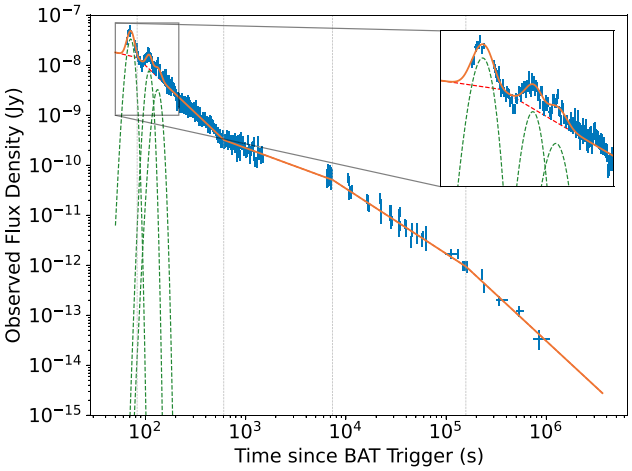

Figure 3. Observed XRT flux density light curve of GRB 210112A is shown in blue, fitted using our code described in Section 3.1. Orange line represents the fitted model; red and green dashed lines are the continuum and flare components, respectively. Grey vertical lines show the power-law breaks. Inset: zoom at 40–320 s showing the early X-ray flaring.

With a set of flares identified, we exclude those data such that we are left with only the afterglow continuum. A series of broken power laws are fitted, each with a different number of breaks up to 5, to cover a range of common afterglow light-curve shapes seen in GRBs (Nousek et al. 2006; O'Brien et al. 2006; Zhang et al. 2006). A least squares method is used to fit the data. For each model, we introduce the Akaike Information Criterion (AIC, Akaike 1974), an estimator of relative model quality. This allows us to use a penalty function to avoid over fitting the continuum. For each fit, we calculate:

$$\Delta\mathrm{AIC} = 2k + N\ln(\mathrm{RSS}), \quad (1)$$

where k is the number of parameters modelled, N the number of data points, RSS is the residual sum of squares, and ΔAIC is the quantity we look to minimize.

We re-add the flare data and subtract the fitted continuum – leaving only residuals and clear flare peaks. For each flare, we fit a fast-rise, exponential-decay curve, commonly found to be a good representation of GRB pulses (Norris et al. 1996; Peng et al. 2010). From this we can find the temporal parameters for each flare, and more usefully, we can integrate across the flare model to derive the X-ray fluence for each flare.

3.2 Flares in GRB 210112A

The light curve fitted with our code is shown in Fig. 3 and the full set of fit parameters are shown Table B1. The burst appears to look like a standard 'canonical' light curve, showing all phases described in Nousek et al. (2006) and Zhang et al. (2006). We find three flares, all occurring during the ongoing prompt emission phase, at times 64.9–89.9, 92.1–125.1, and 126.3–152.8 s (relative to BAT trigger time). All three flares are observed to be coincident in X-ray and gamma-ray, as shown in the joint light curve in Fig. 1, suggesting they are both formed by the same internal process – therefore we attribute the X-ray flares to the prompt emission phase. The X-ray fluence outputs for each flare are shown in Table 1. The code also outputs a fluence error of 3.3×10^{-9}, 6.6×10^{-9}, and 6.8×10^{-9} erg cm^{-2} (0.3–10 keV) for each respective flare, but these are small relative to the later discussed model uncertainties and do not translate to predicted radio flux errors.

Table 1. The flux density of the predicted radio flares, for the three flares of GRB 210112A.

Flare no.	Observed fluence (0.3–10 keV) (erg cm^{-2})	Predicted flux density at 144 MHz (mJy)
1	4.45×10^{-7}	191
2	1.29×10^{-7}	56
3	5.44×10^{-8}	23

There is a possibility of a late time jet break at $t \sim 10^5$ s, our method of an AIC penalty function prefers a model fit with a late-time jet break, and there is a hardening of the afterglow spectrum at this time, as presented in Fig. 2. However, an F-test significance test shows this temporal jet break fit is only significant to a $\sim 1.5\sigma$ significance level, over a broken power-law fit without this break. The spectral hardening at this time is also significant only to $\sim 1.65\sigma$.

GRB 210112A is consistent with the population of LGRBs when plotted on the hardness-duration distribution (Kouveliotou et al. 1993) and the Amati relation (Amati 2006). Taking values from the set of spectral and temporal fits across the evolution, they are consistent with the distribution of parameters of *Swift*-XRT detected GRBs in Evans et al. (2009), and this burst is typical in terms of $N_{\rm H}$, break times, and spectral and temporal indices. Additionally, the properties of each flare are consistent with the population of *Swift* X-ray flares in Yi et al. (2016).

All decay indices and spectral indices are consistent with pre-jet break expectations, taking the end of the XRT data as the earliest possible time for a jet break, we can derive constraints, for $z = 2$, on the jet opening angle θ_j and total energy budget E_γ of this burst. Following the methods of Starling et al. (2009, and references therein), we derive $E_{\rm iso} = 3.62 \times 10^{52}$ erg, and lower limits of $\theta_j \geq 0.143$ rad and $E_\gamma \geq 3.71 \times 10^{50}$ erg; for a flat universe with $H_0 = 67.4$ km s^{-1} Mpc^{-1}, $\Omega_{\rm M} = 0.315$, and $\Omega_{\rm vac} = 0.811$ (Planck Collaboration 2020). These parameter limits are consistent with the population of jet break parameters shown in Zhao et al. (2020).

4 SEARCH FOR COHERENT LOW-FREQUENCY RADIO EMISSION

It is possible to make predictions for the expected radio flux densities if the emission originates in a magnetic wind model, as outlined in Usov & Katz (2000). The relativistic, strongly magnetized winds interact with the ambient medium to produce the observed synchrotron spectrum, as well as low-frequency electromagnetic waves.

4.1 Radio predictions

We test these predictions using LOFAR HBA data, with a central observing frequency of 144 MHz and a bandwidth of 48 MHz. The peak frequency of radio emission is

$$\upsilon_{\rm max} = \frac{1}{1+z}\epsilon_B^{1/2}\,{\rm MHz}\,, \tag{2}$$

where z is the GRB redshift, and ϵ_B is the fraction of total energy in the magnetic field. This parameter is not well defined, and this is discussed later in Section 5, but we take $\epsilon_B = 10^{-3}$, following Katz (1997). For GRB 210112A, with our $z = 2$ assumption, we find a peak frequency of 0.011 MHz. This is well below the capability of current radio facilities, however, LOFAR is sufficient to probe the high-energy tail of this emission.

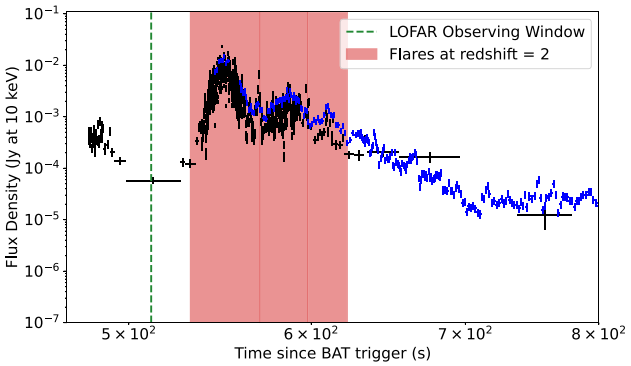

Figure 4. The BAT (black) and XRT (blue) light curve with a dispersion delay applied − for LOFAR 144 MHz HBA observations at $z = 2$, equivalent to a 480 s shift. The green vertical line marks the start of the LOFAR observing window (the end is not displayed on this figure), and red regions mark the flares. At $z = 2$, the dispersion delay is such that all three flares and the plateau lie within the LOFAR observing window.

The radio emission is delayed compared to the analogous prompt pulses, as a result of dispersion through the line of sight. From Taylor & Cordes 1993 (see also Cordes & Lazio 2003), the dispersion delay is given by

$$\tau(\upsilon) \sim \frac{\rm DM}{241\upsilon^2}\,{\rm s}\,, \tag{3}$$

where DM is the dispersion measure and υ the observing frequency in GHz. We expect DM to scale with redshift, but this relation is not well defined. In particular, the contribution of the environment near to the burst and host galaxy is unknown. For a more in-depth discussion of dispersion measure, see Macquart et al. (2020) and James et al. (2022). In this case, we follow Lorimer et al. (2007) and estimate DM as $\sim 1200z$ pc cm^{-3}. Given this, we expect a delay $\tau(\upsilon) = 480$ s, placing all three flares in our LOFAR observation window. Fig. 4 shows the gamma-ray and X-ray data with the corresponding dispersion delay applied.

The observed pulse width will be longer than the intrinsic pulse width after being spread through dispersion. As the pulse occupies a range of frequency, each part will be delayed by a differing amount, spreading the signal. If we model the temporal shape of the intrinsic pulse as a delta function, the observed duration τ_r can be estimated, as given in Usov & Katz (2000):

$$\tau_r \sim 2\frac{\Delta\upsilon}{\upsilon}\tau(\upsilon)\,{\rm s}\,, \tag{4}$$

where $\Delta\upsilon$ is the observing bandwidth in GHz and $\tau(\upsilon)$ the dispersion delay given in equation (3). The real intrinsic pulse will have some finite length so the observed radio pulse should actually be longer, the peak radio emission should occur in the time period τ_r.

Finally, we can calculate the radio spectral flux density for a radio pulse, based on the X-ray fluence of the XRT flares. Given by Usov & Katz (2000), the flux in the dispersion limited and non-dispersion limited cases for each flare are given as:

$$F_\upsilon = \begin{cases} \frac{\delta(\beta-1)}{\tau_r \upsilon_{\rm max}}\left(\frac{\upsilon}{\upsilon_{\rm max}}\right)^{-\beta}\frac{\Phi_\gamma}{10^{-23}}\,{\rm Jy}, & \tau_r \leq \frac{2\Delta\upsilon}{\upsilon}\tau(\upsilon) \\ \frac{\delta(\beta-1)}{2\Delta\upsilon\tau}\left(\frac{\upsilon}{\upsilon_{\rm max}}\right)^{1-\beta}\frac{\Phi_\gamma}{10^{-23}}\,{\rm Jy}, & \tau_r > \frac{2\Delta\upsilon}{\upsilon}\tau(\upsilon) \end{cases}, \tag{5}$$

where δ is the ratio of bolometric radio fluence to bolometric gamma-ray fluence; β is the power-law index in the high-frequency radio tail; τ_r is the intrinsic flare length, and Φ_γ is the bolometric gamma-ray fluence. Following Starling et al. (2020) and references therein, we

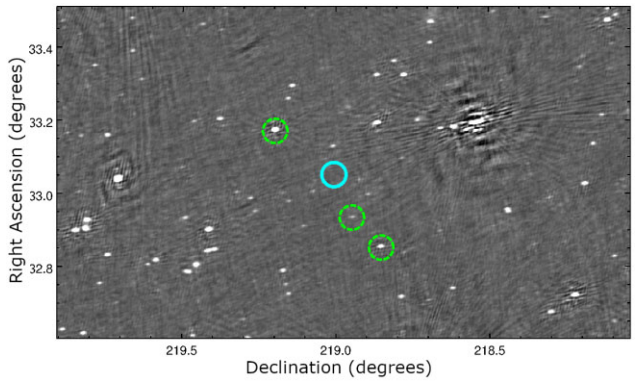

Figure 5. The full-time LOFAR image spanning the full 7199 s of observation, showing GRB 210112A and the surrounding region. The blue circle shows the position of the GRB and dashed green circles show a select few comparison sources. The size of the circles are 2 arcmin and are meant only to guide the eye.

take $\delta \sim 0.1\epsilon_B$ and $\beta \sim 1.6$. For the three X-ray flares identified in Section 3.2, we obtain the radio fluence predictions in Table 1.

Dense regions around the progenitor and in the line-of-sight may block emission where the plasma is opaque to the low-frequency radio emission. This frequency is dependent upon the number density of electrons in the plasma. Zhang (2014) estimate the co-moving plasma frequency in the shocked ejecta region of the blast wave as ∼4 MHz, which is comfortably below our observation band, so we expect the emission to escape along the jet axis. Another effect that can contribute to low-frequency propagation is the interaction of low-frequency radiation and electrons, leading to free–free absorption. Adopting a free–free turnover of 300 MHz (Lyutikov, Burzawa & Popov 2016; Piro 2016), this would lie at 100 MHz in our observed band for $z = 2$, below the minimum observation frequency, and hence free–free absorption is not expected to heavily impact emission at 144 MHz.

4.2 Radio results

The large-scale radio image generated from the full time 2 h observation is shown in Fig. 5, showing the surrounding region, position of our GRB and position of several bright comparison sources. Source extraction was performed using TRAP (version 5.0, Swinbank et al. 2015), using a force fit extraction monitor at the position of our GRB and comparison sources, using default settings and restoring beam shape. These positions are monitored at each timeslice in our 60 and 320 s snapshot images. Fig. 6 shows the resultant light curve of these snapshot images, marked with the expected arrival time of the radio flares. At the position of GRB 210112A, however, we do not detect significant radio emission.

TRAP outputs an rms value, calculated with the inner default 1/8th of the image, centred on the GRB. Given the non-detection of radio emission at our GRB position, we use this output rms value of 14 mJy for our 320 s snapshot image. We therefore calculate the 3σ (3x rms) upper limit on any flaring activity at this integration length to be 42 mJy. The flare may be split across multiple time bins, if the bin does not line up exactly with when the flare starts and ends, meaning the flare could be smeared out – at worst it is split evenly across two bins. Carbone et al. (2017) and Chastain, van der Horst & Carbone (2022) perform simulations and discuss how this could affect transient searches. However, in the case of the first flare at least, the radio flux should be bright enough to always be visible in each bin.

Additionally, we image with 60 s snapshots which would catch a flare split across multiple bins, and to look for any shorter timescale variations in the data. In these images, we also detect no source at the expected position. We obtain an rms noise of 29 mJy and consequently a 3σ upper limit of 87 mJy.

The predicted flux of the brightest radio flare lie well above the rms noise in the data for both time intervals, thus we can confidently say the flare predicted by the model would be seen provided the input assumptions are correct.

We use the full 2 h duration image to calculate a similar 3σ flux density limit. Any predicted flares are covered by integrating noise in these images, but this deep image allows us to put a limit on persistent emission from the region – for example from star formation within the host galaxy. For this, we yield an upper limit of 3 mJy.

We also measure the flux density for three comparison sources in the field indicated in the full images, using the same 320 s snapshot intervals. Fig. 7 shows we recover the brightest of three sources in all images. The two fainter comparison sources are not recoverable in time-sliced data, and this is consistent with the measured rms for this choice of binning.

5 DISCUSSION

Our search for coherent radio emission has therefore resulted in no detections for any flares. The 3 mJy limit on the GRB position obtained from the full two hour image may be reasonably compared to those for long GRB 180706A. Our 2 h observation 3σ upper limit is 1.76 times higher than that found for GRB 180706A using the same instrument and approach (Rowlinson et al. 2019). A forced fit at the position of GRB 180706A found a 1σ flux density excess of 1.1 ± 0.9 mJy, which would not be recoverable in the data set of GRB 210112A, while it still represents one of the best constraints available at present.

The sensitivity of our observations was sufficient to have seen the first predicted radio flare described by the Usov & Katz (2000) magnetic wind model, analogous to the inner engine pulsing/flaring activity. The lack of detection could suggest that this mechanism is not occurring, or alterations to our assumptions are required. One of the model dependencies is the fraction of energy in the magnetic field, and following the assumptions of the magnetic wind model this is assumed to be $\epsilon_B = 10^{-3}$ (Katz 1997). If we instead make a more conservative estimate of $\epsilon_B \lesssim 10^{-4}$ we would predict radio emission to peak in brightness at ∼19 mJy, approximately the rms noise in the images, and thus would not expect to see the radio pulses in this case. This suggests that our non-detection may favour a lower fraction of energy in the magnetic field for this GRB. In the case of rapid radio follow-up of long GRB 210419A, the non-detection of emission related to X-ray flares results in an upper limit corresponding to a constrain of $\epsilon_B \lesssim 10^{-3}$ (Tian et al. 2022b). In a recent search for coherent radio emission from SGRBs, Tian et al. (2022a) suggest constraints of $\epsilon_B \lesssim 2 \times 10^{-4}$ in the GRB jet from similar arguments. A wide range of values between 10^{-5} and 0.33 have been estimated for pre-*Swift* GRBs predominantly through afterglow light curve modelling (Panaitescu & Kumar 2001; Santana, Barniol Duran & Kumar 2014), and this has been extended down to 10^{-8} in a *Swift* study (Santana et al. 2014). It is one of the hardest parameters to pin down using afterglow modelling, using different methods on the same data set can yield quite different results.

Certainly, the greatest uncertainty lies in the redshift estimate. In this case, the lack of a spectroscopic redshift leads us to adopt a

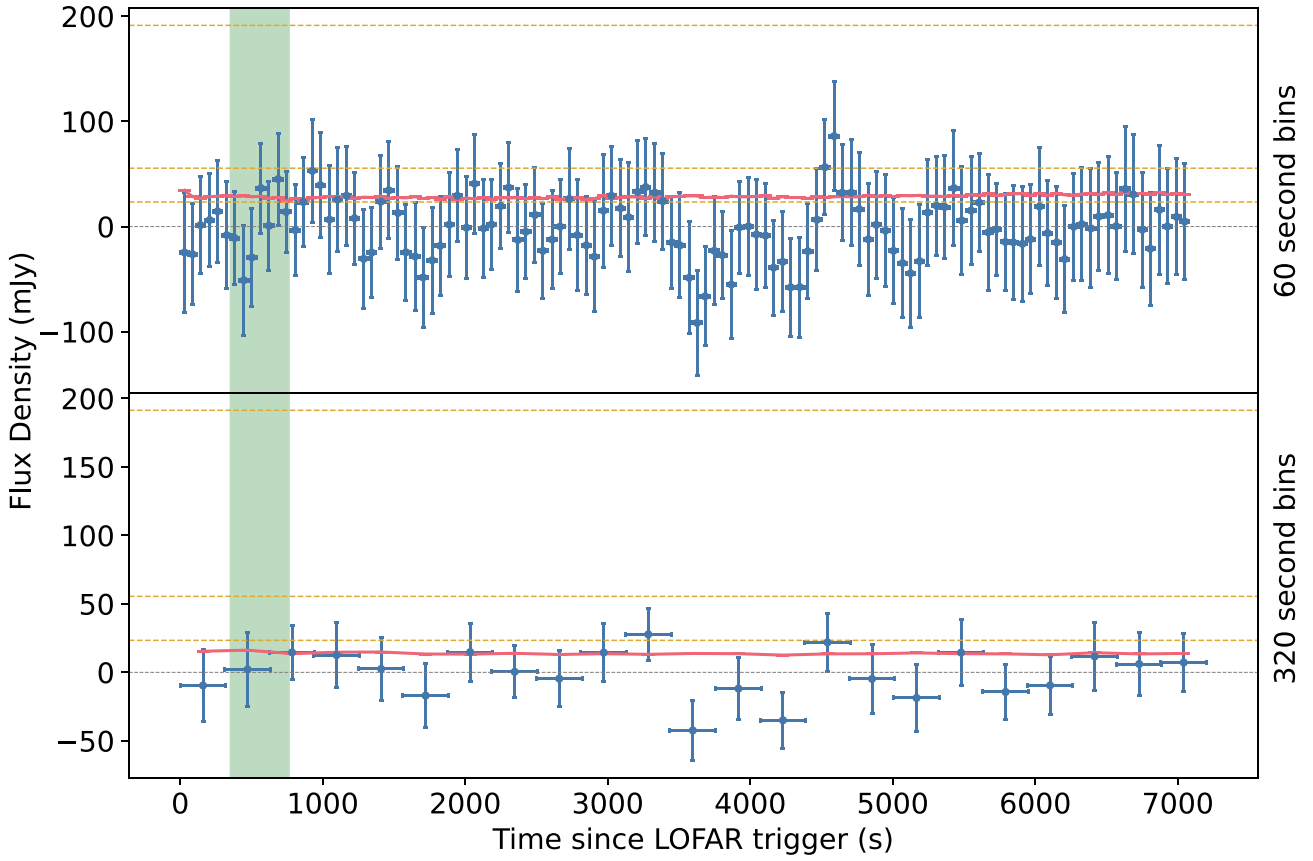

Figure 6. The observed 144 MHz radio flux at the position of GRB 210112A as a function of time. We show data from images created with 60 s bins and 320 s bins. The red line shows the 1σ rms noise measured in each image, calculated from the inner 1/8th of the image. The yellow dotted lines show the expected flux density values for the three X-ray flares predicted in Section 4. The green shaded region shows the expected time of arrival of all three radio pulses for $z = 2$, the dispersed signals cause all three to overlap.

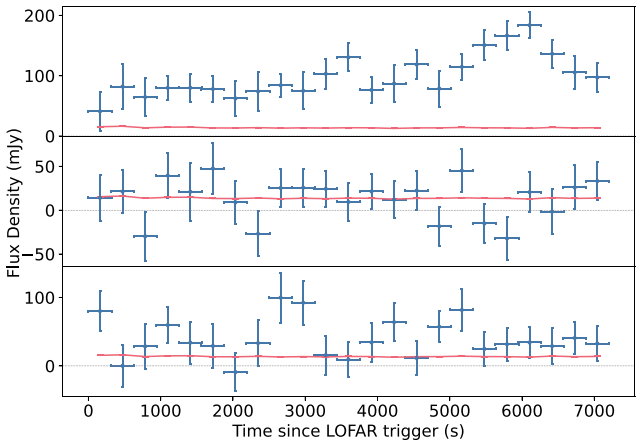

Figure 7. The observed 144 MHz radio flux at the position of several comparison sources in the same observation field as GRB 210112A, as shown in Fig. 5, as a function of time. Images are created with 320 s bins. Shown on the bottom two sub-figures are the rms noise in the images, in red. The top figure shows a source significantly brighter than the noise even in these snapshot images.

redshift value of $z = 2$ from multi-colour afterglow photometry (Kann et al. 2021a), which happens to lie at approximately the mean redshift for *Swift* long GRBs (Evans et al. 2009). This has implications on the observed brightness and, importantly, the duration and timing of the flares. We calculated the smallest redshift that would allow us to still observe the peak of the first flare, and this is $z = 1.914$, smaller values would cutoff part of the predicted pulse and the expected brightness would drop below the noise threshold. The similar limit for the third flare is $z = 1.637$, but we show this flare would not be observable regardless, given the noise in the image. The upper limit of redshift on our observations extends far beyond our assumed value: the LOFAR window extends to cover a much broader range of dispersion delays, but at $z \sim 6$, we expect the radio flux to drop below our sensitivity thresholds. We therefore examined the host galaxy through published photometry and additional observations with the DOT telescope (Section 2.3). We used the CODE INVESTIGATING GALAXY EMISSION (CIGALE, Boquien et al. 2019) package to evaluate the galaxy's SED. CIGALE uses a series of additive templates to simulate the full emission of a galaxy and here we use a double exponential star formation history and a low metallicity stellar population (Bruzual & Charlot 2003) to model the starburst galaxies typical of LGRB hosts. Dust attenuation was included using the Calzetti et al. (2000) extinction law and CIGALE assumes the cosmology identified by the Seven-year *Wilkinson Microwave Anisotropy Probe* observations ($H_0 = 70.4$ km s^{-1} Mpc^{-1} and $\Omega_M = 0.272$; Komatsu et al. 2011). CIGALE creates a grid of models across the combined parameter space of the component templates and uses Bayesian inference to derive the most likely values for each parameter. We initially allowed the redshift to vary between 0.5 and 2.5, finding it tended towards a

lower redshift of $z \sim 1.3$ but this is poorly constrained and likely to be unreliable. We therefore assumed a fixed redshift of $z = 2$ from Kann et al. (2021a) and found it to be compatible with the host data. We infer a stellar mass of $\log(M_*/M_\odot) \sim 10.9$, a star formation rate of $\sim 40\,M_\odot\,\mathrm{yr}^{-1}$ and a dust extinction of $E(B-V) \sim 0.1$, properties generally consistent with the known LGRB host population (e.g. Levesque 2014; Stanway, Levan & Davies 2014). We note, however, that these values are generally not tightly constrained due to the narrow wavelength range of our host galaxy photometry. This star formation rate can also be used to derive an estimate of the expected 150 MHz flux density. Following the prescription of Gürkan et al. (2018) we find a value of ∼0.015 mJy, which aligns well with our non-detection of persistent emission in the 2-h HBA observation in which the limiting flux density is 3 mJy.

Currently LOFAR is limited to use either 48 HBA or 48 equivalent Low Band Antenna (LBA) at a time, and thus our rapid response observations only make use of the HBA. In this case, we are further from the peak radio frequency, but the sensitivity is considerably better such that it is worth the trade-off. The upgrades to LOFAR 2.0 in the future will allow 96 antennas with simultaneous observations using both bands (Hessels et al., in prep). The LBA operates at 10–90 MHz meaning we can probe closer to the predicted radio flux peak at ∼1 MHz. Given this, in the case of GRB 210112A, we should expect to observe at least the brightest flare even with the sensitivity of LBA not being quite as deep as HBA. The rapid response constraints also loosen for a lower observing frequency, where the same $z = 2$ dispersion delay applied to LBA is 3415 s, placing it in the middle of our LOFAR observing window. A detection in both frequencies for a given equivalent X-ray flare may allow us to begin to constrain the β parameter, the high-frequency tail power-law index.

Going forward, it is clear that with uncertain model parameters, uncertain redshift, and the unpredictability of X-ray flares occurring during the LOFAR observation, if any occur at all for a given GRB, that the best strategy is to observe a large sample of bursts in this way. Sample parameter distributions can therefore be folded through the observed flux limit distributions, to give proper statistics.

6 CONCLUSION

In this paper, we present the observations of GRB 210112A made with LOFAR's HBA in rapid response mode. We test a magnetic wind model, where we look for predicted low-frequency coherent radio emission associated with the prompt phase gamma-ray pulses and X-ray flares. A detection at the predicted time would evidence the GRB jet is Poynting flux dominated. Using LOFAR HBA observations, we expect to at least see the first flare given the model and redshift assumptions.

However, no emission is detected at the position of the GRB on short imaging time-scales. We also probe the full 2 h observation for any persistent emission and produce a 3 mJy upper limit, which is consistent with the expected emission from a typical LGRB host galaxy at a redshift of 2.

A non-detection in one or a few sources does not necessarily rule out this magnetic wind model. We have discussed uncertainties in our assumptions and the model itself. The redshift is obtained tentatively, through multi-colour afterglow photometry, though it is consistent with spectral fitting and host galaxy template fitting. The effect of redshift is primarily on the predicted duration and timing of the radio flares. At $z < 1.91$, the brightest flare would fall before our observation window. Our search is optimized for $z = 2$, but if this differs then it has implications on our sensitivity to a dispersed signal of a different length. Additionally, the emission models and input parameters still remain uncertain. Changes in the strength of magnetic field or efficiency of the emission mechanisms means less radio emission is expected, possibly low enough to not be detected in our images. At $\epsilon_B = 10^{-4}$, the predicted radio flux would be below the image noise in our observations.

To confidently test the prediction of radio emission from a magnetic wind model, we need several rapid follow-up observations of GRBs, simultaneous with *Swift* or similar X-ray prompt follow-up, and with spectroscopic redshifts. Given our assumed DM $= 1200z$, z is directly proportional to the dispersion delay of radio pulses. Hence, a response time of 5 min after the initial *Swift*-BAT trigger allows us to probe radio emissions to bursts at $z > 1$. This hard limit is relaxed slightly further as we probe the more accessible X-ray flares, which usually occur in the first few hundred seconds of the GRB, during or after the prompt emission. The Space Variable Objects Monitor (Atteia, Cordier & Wei 2022) mission is expected to launch mid 2023. The ECLAIRs (Godet et al. 2014) telescope onboard will provide GRB triggers at a low energy threshold of 4 keV, lower than that of existing missions. This will provide access to the soft X-ray regime of prompt emissions, cementing the links between X-ray flare and gamma-ray pulses. In particular, with LOFAR 2.0 rapid observations, we will be able to probe multiple radio frequency channels simultaneously.

ACKNOWLEDGEMENTS

We thank the referee Jonathan Katz for critically reviewing this work. The LOFAR data were taken under programme LC15_013 (PI Starling). AH was supported by an STFC studentship. RLCS acknowledges support from an ASTRON Helena Kluyver visiting fellowship. AR acknowledges funding from the Dutch Research Council (NWO) Aspasia grant (number: 015.016.033). IdR acknowledges support through the project CORTEX (NWA.1160.18.316) of the research programme NWA-ORC which is (partly) financed by the NWO. RAJE-F acknowledges support from the UK Space Agency and the European Union's Horizon 2020 Programme under the AHEAD2020 project (grant agreement number 871158). NS was funded by a University of Leicester SURE internship. KW acknowledges support through a UK Research and Innovation Future Leaders Fellowship awarded to Dr B. Simmons (MR/T044136/1). This work made use of data supplied by the UK *Swift* Science Data Centre at the University of Leicester. We thank the staff of the 3.6m Devasthal Optical Telescope (DOT), an optical telescope run and managed by Aryabhatta Research Institute of Observational Sciences (ARIES), an autonomous Institute under the Department of Science and Technology, Government of India, for service observations with the ADFOSC instrument. This paper is based (in part) on data obtained with the International LOFAR Telescope (ILT) under project code LC10 012. LOFAR is the Low Frequency Array designed and constructed by ASTRON. It is observing data processing and data storage facilities in several countries, that are owned by various parties (each with their own funding sources), and that are collectively operated by the ILT foundation under a joint scientific policy. The ILT resources have benefitted from the following recent major funding sources: Institut National des Sciences de l'Univers (CNRS-INSU), Observatoire de Paris and Université d'Orléans, France; Bundesministerium für Bildung und Forschung (BMBF), Ministerium für Kultur und Wissenschaft des Landes Nordrhein-Westfalen (MIWF-NRW), Max Planck Society (MPG), Germany; Science Foundation Ireland (SFI), Department of Business, Enterprise and Innovation (DBEI), Ireland; NWO, The Netherlands; The Science and Technology Facilities Council, UK; Ministry of Science and Higher Education, Poland.

DATA AVAILABILITY

LOFAR data are available in the LOFAR Long-Term Archive (LTA) at https://lta.lofar.eu. *Swift* data and XRT products are available via the UK Swift Science Data Centre (UKSSDC) at www.swift.ac.uk.

REFERENCES

Abbott B. P. et al., 2017, ApJ, 848, L13
Abdo A. A. et al., 2009, ApJ, 706, L138
Akaike H., 1974, IEEE Trans. Autom. Control, 19, 716
Amati L., 2006, MNRAS, 372, 233
Ambrosi E. et al., 2021, GCN Circ., 29289, 1
Anderson G. E. et al., 2018, MNRAS, 473, 1512
Anderson G. E. et al., 2021, Publ. Astron. Soc. Aust., 38, e026
Arnaud K. A., 1996, Astron. Soc. Pac. Conf. Ser. 101, 17
Atteia J. L., Cordier B., Wei J., 2022, Int. J. Mod. Phys. D, 31, 2230008
Barbary K., 2018, Astrophysics Source Code Library, record(ascl:1811.004)
Barthelmy S. D. et al., 2005, Space Sci. Rev., 120, 143
Beniamini P., Granot J., 2016, MNRAS, 459, 3635
Bernardini M. G., 2015, J. High Energy Astrophys., 7, 64
Bertin E., Arnouts S., 1996, A&AS, 117, 393
Boquien M., Burgarella D., Roehlly Y., Buat V., Ciesla L., Corre D., Inoue A. K., Salas H., 2019, A&A, 622, A103
Bruzual G., Charlot S., 2003, MNRAS, 344, 1000
Burrows D. N. et al., 2005, Space Sci. Rev., 120, 165
Calzetti D., Armus L., Bohlin R. C., Kinney A. L., Koornneef J., Storchi-Bergmann T., 2000, ApJ, 533, 682
Carbone D., van der Horst A. J., Wijers R. A. M. J., Rowlinson A., 2017, MNRAS, 465, 4106
Chastain S. I., van der Horst A. J., Carbone D., 2022, Astron. Comput., 40, 100629
Chincarini G. et al., 2007, ApJ, 671, 1903
Cordes J. M., Lazio T. J. W., 2003, preprint (astro–ph/0301598)
Costa E. et al., 1997, Nature, 387, 783
Dessenne C. A. C. et al., 1996, MNRAS, 281, 977
Dimple Misra K., Ghosh A., Gupta R., Kumar A., Pandey S. B., 2021, GCN Circ., 29333, 1
Drenkhahn G., Spruit H. C., 2002, A&A, 391, 1141
Duque R., Beniamini P., Daigne F., Mochkovitch R., 2022, MNRAS, 513, 951
Evans P. A. et al., 2009, MNRAS, 397, 1177
Evans P. A. et al., 2010, A&A, 519, A102
Evans P. A. et al., 2021, GCN Circ., 29295, 1
Falcone A. D. et al., 2007, ApJ, 671, 1921
Fan Y. Z., Wei D. M., 2005, MNRAS, 364, L42
Frail D. A., Kulkarni S. R., Nicastro L., Feroci M., Taylor G. B., 1997, Nature, 389, 261
Galama T. J. et al., 1998, Nature, 395, 670
de Gasperin F. et al., 2019, A&A, 622, A5
Gehrels N. et al., 2004, ApJ, 611, 1005
Goad M. R., Osborne J. P., Beardmore A. P., Evans P. A., Team. Swift-XRT, 2021, GCN Circ., 29290, 1
Godet O. et al., 2014, in Takahashi T., den Herder J.-W. A., Bautz M.eds, SPIE Conf. Ser., vol. 9144, Space Telescopes and Instrumentation 2014: Ultraviolet to Gamma Ray. SPIE, Bellingham, p. 914424
Gourdji K., Rowlinson A., Wijers R. A. M. J., Goldstein A., 2020, MNRAS, 497, 3131
Guidorzi C., Dichiara S., Frontera F., Margutti R., Baldeschi A., Amati L., 2015, ApJ, 801, 57
Gupta R., Kumar A., Dimple, Ghosh A., Chand K., Aryan A., Pandey S. B., Misra K., 2021, GCN Circ., 29301, 1
Gürkan G. et al., 2018, MNRAS, 475, 3010
High Nasa 2014, Astrophysics Source Code Library, record(ascl:1408.004)
Hjorth J. et al., 2003, Nature, 423, 847
Hu Y.-D., Liang E.-W., Xi S.-Q., Peng F.-K., Lu R.-J., Lü L.-Z., Zhang B., 2014, ApJ, 789, 145
Intema H. T., Jagannathan P., Mooley K. P., Frail D. A., 2017, A&A, 598, A78
James C. W., Prochaska J. X., Macquart J. P., North-Hickey F. O., Bannister K. W., Dunning A., 2022, MNRAS, 509, 4775
Kann D. A., de Ugarte Postigo A., Thoene C. C., Blazek M., Agui Fernandez J. F., Sota A., 2021a, GCN Circ., 29296, 1
Kann D. A., de Ugarte Postigo A., Thoene C. C., Blazek M., Agui Fernandez J. F., Sota A., 2021b, GCN Circ., 29300, 1
Kann D. A., de Ugarte Postigo A., Thoene C. C., Blazek M., Agui Fernandez J. F., Vico Linares J. I., 2021c, GCN Circ., 29319, 1
Kaplan D. L. et al., 2015, ApJ, 814, L25
Katz J. I., 1997, ApJ, 490, 633
Komatsu E. et al., 2011, ApJS, 192, 18
Koranyi D. M., Green D. A., Warner P. J., Waldram E. M., Palmer D. M., 1995, MNRAS, 276, L13
Kouveliotou C., Meegan C. A., Fishman G. J., Bhat N. P., Briggs M. S., Koshut T. M., Paciesas W. S., Pendleton G. N., 1993, ApJ, 413, L101
Kumar B. et al., 2018, Bull. Soc. R. Sci. Liege, 87, 29
Lattimer J. M., Schramm D. N., 1976, ApJ, 210, 549
Levesque E. M., 2014, PASP, 126, 1
Lorimer D. R., Bailes M., McLaughlin M. A., Narkevic D. J., Crawford F., 2007, Science, 318, 777
Lyutikov M., Burzawa L., Popov S. B., 2016, MNRAS, 462, 941
Macquart J. P. et al., 2020, Nature, 581, 391
Misra K., Ghosh A., Gupta R., Kumar A., Pandey S. B., 2021, GCN Circ., 29333, 1
Moroianu A., Wen L., James C. W., Ai S., Kovalam M., Panther F. H., Zhang B., 2023, Nat. Astron., 7, 579
Norris J. P., Nemiroff R. J., Bonnell J. T., Scargle J. D., Kouveliotou C., Paciesas W. S., Meegan C. A., Fishman G. J., 1996, ApJ, 459, 393
Nousek J. A. et al., 2006, ApJ, 642, 389
Novichonok A., Belkin S., Pozanenko A., Ehgamberdiev S., IKI GRB, 2021, GCN Circ., 29292, 1
O'Brien P. T., Willingale R., Osborne J. P., Goad M. R., 2006, New J. Phys., 8, 121
Offringa A. R., de Bruyn A. G., Biehl M., Zaroubi S., Bernardi G., Pandey V. N., 2010, MNRAS, 405, 155
Offringa A. R., van de Gronde J. J., Roerdink J. B. T. M., 2012, A&A, 539, A95
Offringa A. R. et al., 2014, MNRAS, 444, 606
Omar A., Kumar T. S., Krishna Reddy B., Pant J., Mahto M., 2019, Current Science, 116, 1472
Panaitescu A., Kumar P., 2001, ApJ, 560, L49
Pankov N., Pozanenko A., Klunko E., Belkin S., IKI GRB, 2021, GCN Circ., 29302, 1
Peng Z. Y., Yin Y., Bi X. W., Zhao X. H., Fang L. M., Bao Y. Y., Ma L., 2010, ApJ, 718, 894
Piro A. L., 2016, ApJ, 824, L32
Planck Collaboration, 2020, A&A, 641, A6
Rees M. J., Meszaros P., 1994, ApJ, 430, L93
Roming P. W. A. et al., 2005, Space Sci. Rev., 120, 95
Rossi A., Kann D. A., CIBO Collaboration, , 2021, GCN Circ., 29456, 1
Rowlinson A., Anderson G. E., 2019, MNRAS, 489, 3316
Rowlinson A. et al., 2019, MNRAS, 490, 3483
Rowlinson A. et al., 2021, MNRAS, 506, 5268
Santana R., Barniol Duran R., Kumar P., 2014, ApJ, 785, 29
Schlafly E. F., Finkbeiner D. P., 2011, ApJ, 737, 103
Siegel M. H., Team Ambrosi Swift/UVOT, 2021, GCN Circ., 29303, 1
Stamatikos M. et al., 2021, GCN Circ., 29297, 1
Stanway E. R., Levan A. J., Davies L. J. M., 2014, MNRAS, 444, 2133
Starling R. L. C. et al., 2009, MNRAS, 400, 90
Starling R. L. C., Rowlinson A., van der Horst A. J., Wijers R. A. M. J., 2020, MNRAS, 494, 5787
Svinkin D. et al., 2021, GCN Circ., 29315, 1
Swinbank J. D. et al., 2015, Astron. Comput., 11, 25
Taylor J. H., Cordes J. M., 1993, ApJ, 411, 674
Tian J. et al., 2022a, Publ. Astron. Soc. Aust., 39, e003
Tian J. et al., 2022b, MNRAS, 514, 2756

Tingay S. J. et al., 2013, Publ. Astron. Soc. Aust., 30, e007
Totani T., 2013, PASJ, 65, L12
Ursi A. et al., 2021, GCN Circ., 29293, 1
Usov V. V., Katz J. I., 2000, A&A, 364, 655
van Haarlem M. P. et al., 2013, A&A, 556, A2
van Paradijs J. et al., 1997, Nature, 386, 686
van Weeren R. J. et al., 2016, ApJS, 223, 2
Wayth R. B. et al., 2018, Publ. Astron. Soc. Aust., 35, e033
Williams W. L. et al., 2016, MNRAS, 460, 2385
Willingale R., Starling R. L. C., Beardmore A. P., Tanvir N. R., O'Brien P. T., 2013, MNRAS, 431, 394
Wilms J., Allen A., McCray R., 2000, ApJ, 542, 914
Woosley S. E., MacFadyen A. I., 1999, A&AS, 138, 499
Yi S.-X., Xi S.-Q., Yu H., Wang F. Y., Mu H.-J., Lü L.-Z., Liang E.-W., 2016, ApJS, 224, 20
Zhang B., 2014, ApJ, 780, L21
Zhang B., Mészáros P., 2001, ApJ, 552, L35
Zhang B., Fan Y. Z., Dyks J., Kobayashi S., Mészáros P., Burrows D. N., Nousek J. A., Gehrels N., 2006, ApJ, 642, 354
Zhao W. et al., 2020, ApJ, 900, 112
Zheng C. et al., 2021, GCN Circ., 29326, 1

APPENDIX A: SPECTRAL FITS

Table A1. Time coverage and spectral fits for all timesliced phases of BAT and XRT data. Where there is simultaneous coverage, fits are performed with a broken power law covering both sets of data. In these cases, Γ_1 the lower energy photon index and Γ_2 the higher energy photon index. Errors shown are 90 per cent confidence intervals. BAT only phases are fitted with a cutoff power law. XRT only phases are fitted with a double absorbed power law. **Phase 4** is the spectral fit used to constrain and freeze the intrinsic absorption parameter to 2.980×10^{22} cm^{-2}.

Phase	Instrument(s)	Start (s)	Stop (s)	Γ_1	Γ_2	Chi-square/degrees of freedom
Preflare	BAT	0	37.72	–	$0.67^{+0.36}_{-0.41}$	63.18/55
Flare 1	BAT	37.72	89.94	–	$1.20^{+0.02}_{-0.03}$	33.95/55
Flare 1 rise	BAT	37.72	65.48	–	$1.16^{+0.03}_{-0.07}$	48.89/55
Flare 1 peak	BAT	65.48	75.91	–	$1.15^{+0.02}_{-0.06}$	23.94/55
Flare 1 decay	BAT, XRT	78.35	89.94	$0.83^{+0.06}_{-0.06}$	$1.74^{+0.05}_{-0.05}$	450.67/607
Flare 2	BAT, XRT	89.61	117.8	$0.85^{+0.03}_{-0.03}$	$1.72^{+0.04}_{-0.04}$	727.31/792
Flare 3	BAT, XRT	117.8	153	$0.48^{+0.13}_{-0.16}$	$1.54^{+0.02}_{-0.02}$	679.08/653
Phase 2	BAT, XRT	153	614	$1.77^{+0.04}_{-0.04}$	$2.22^{+0.06}_{-0.05}$	743.80/774
Phase 3 WT	XRT	614	935	$2.34^{+1.16}_{-1.14}$	–	0.59/3
Phase 3 PC	XRT	935	8913	$1.96^{+0.05}_{-0.05}$	–	273.47/365
Phase 4	**XRT**	**8913**	**1.70×10^5**	**$2.15^{+0.05}_{-0.05}$**	**–**	**419.08/413**
Phase 5	XRT	1.70×10^5	1.08×10^6	$1.74^{+0.28}_{-0.26}$	–	405.04/429

APPENDIX B: TEMPORAL FITS

Table B1. Temporal fits corresponding to Fig. 3. Phase 0 is poorly fit as there are few data points remaining for continuum fitting after flaring data has been excluded.

Canonical phase	Temporal index α	Post-phase break time (s)
Phase 0	0.49 ± 0.95	83.68 ± 318.6
Phase 1	1.91 ± 0.03	604.8 ± 23.2
Phase 2	0.73 ± 0.03	7333 ± 1237
Phase 3	1.30 ± 0.05	157574 ± 67602
Phase 4	1.86 ± 0.34	–
Normalization		$1.14\ (\pm 0.04) \times 10^{-7}$
Chi-square		318.6
Reduced chi-square		1.3

APPENDIX C: OPTICAL DATA

Table C1. Table showing the optical data plotted in Fig. 1 from several observatories.

Telescope	Filter	Time since BAT trigger (days)	Magnitude (AB)	Flux (μJy)	Reference
OSN	Rc	0.126	22.41 ± 0.12	3.44 ($\pm$ 0.36)	Kann et al. (2021a)
OSN	Ic	0.126	21.10 ± 0.075	9.44 ($\pm$ 0.63)	Kann et al. (2021b)
Mondy	Rc	0.807	>22.40	<3.38	Pankov et al. (2021)
DFOT	Rc	0.937	>22.69	<2.59	Gupta et al. (2021)
OSN	Ic	1.13	23.02 ± 0.217	1.61 ($\pm$ 0.29)	Kann et al. (2021b)
DOT	*i*'	1.93	23.19 ± 0.166	1.98 ($\pm$ 0.28)	Dimple et al. (2021)
CAHA	Ic	5.17	23.52 ± 0.19	1.02 ($\pm$ 0.16)	Rossi et al. (2021)
LBT	*z*'	24.3	23.38 ± 0.15	1.62 ($\pm$ 0.21)	Rossi et al. (2021)
LBT	*r*'	24.3	23.96 ± 0.15	0.98 ($\pm$ 0.13)	Rossi et al. (2021)
DOT	*r*'	771.0	23.89 ± 0.117	1.05 ($\pm$ 0.11)	*this work*
DOT	*i*'	771.0	23.67 ± 0.231	1.27 ($\pm$ 0.25)	*this work*
DOT	*z*'	778.0	23.35 ± 0.231	1.66 ($\pm$ 0.34)	*this work*

This paper has been typeset from a TEX/LATEX file prepared by the author.